Experimental investigation of a bipartite quench in a 1D Bose gas

Léa Dubois[1], Guillaume Thémèze[1], Jérôme Dubail[2] and Isabelle Bouchoule[1]

1 Laboratoire Charles Fabry, Institut d'Optique, CNRS, Université Paris-Saclay
2 CESQ and ISIS (UMR 7006), University of Strasbourg and CNRS, 67000 Strasbourg, France

⋆ lea.dubois@universite-paris-saclay.fr

Abstract

Long wavelength dynamics of 1D Bose gases with repulsive contact interactions can be captured by Generalized HydroDynamics (GHD) which predicts the evolution of the local rapidity distribution. The latter corresponds to the momentum distribution of quasiparticles, which have infinite lifetime owing to the integrability of the system. Here we experimentally investigate the dynamics for an initial situation that is the junction of two semi-infinite systems in different stationary states, a protocol referred to as 'bipartite quench' protocol. More precisely we realise the particular case where one half of the system is the vacuum state. We show that the evolution of the boundary density profile exhibits ballistic dynamics obeying the Euler hydrodynamic scaling. The boundary profiles are similar to the ones predicted with zero-temperature GHD in the quasi-BEC regime, with deviations due to non-zero entropy effects. We show that this protocol, provided the boundary profile is measured with infinite precision, permits to reconstruct the rapidity distribution of the initial state. For our data, we extract the initial rapidity distribution by fitting the boundary profile and we use a 3-parameter Ansatz that goes beyond the thermal assumption. Finally, we investigate the local rapidity distribution inside the boundary profile, which, according to GHD, presents, on one side, features of zero-entropy states. The measured distribution shows the asymmetry predicted by GHD, although unelucidated deviations remain.

1   Introduction

Gaining insight on the out-of-equilibrium dynamics of many-body quantum systems is tremendously difficult and is the goal of an active research field. One particular class of systems where important progress has been made over the past decade is the class of integrable one-dimensional systems. Owing to their infinite number of local conserved charges, the description of the local properties of stationary states that arise after relaxation requires a whole function, the rapidity distribution [1–7]. This function can be viewed as the velocity distribution of the infinite-lifetime quasi-particles in the system. Its large-scale effective dynamics is described by generalized hydrodynamics (GHD) [8, 9] (for recent reviews, see e.g. [10, 11]), which assumes local relaxation to a local stationary state. As with any hydrodynamic theory, the most paradigmatic situation that can be handled by GHD is the 'Riemann problem' [12], also dubbed 'bipartite quench' more recently [13–18], or 'domain-wall quench' or 'domain-wall protocol' [19–27]. In this 'bipartite quench protocol', the microscopic dynamics is governed by a translation-invariant Hamiltonian but the initial state is the junction of two semi-infinite homogeneous systems each prepared in a different stationary state of the Hamiltonian. The GHD theory predicts that, at times long enough such that diffusion effects become negligible [28] and Euler-scale hydrodynamics is valid, the time evolution is ballistic. An interesting feature of this protocol is that the local state, within the boundary, is expected to present features characteristic of zero-temperature systems. Thus, this protocol could be used to reveal power-law singularities of correlation functions characteristic of a zero-temperature Luttinger liquid [13], provided a local probe is used.

In this paper, we experimentally realize an instance of the bipartite quench protocol using an ultra-cold atomic Bose gas, well described by the Lieb-Liniger model of one-dimensional Bosons with contact repulsive interactions [29, 30], which is an integrable model. In our experiment, the bipartition consists of the junction of a gas in a stationary state on one side, and the vacuum on the other side. This is in contrast with another bipartite quench protocol realized very recently in the Lieb-Liniger gas in Ref. [31]. There, a completely different method is used, which allows to create an initial state with different non-vanishing densities on the left and on the right. In our work, the initial state is prepared by producing a homogeneous atomic cloud and by removing suddenly its left part. For different evolution times, we record the density profile of the boundary between the two regions, dubbed the boundary profile. We find that the boundary profile exhibits a ballistic behavior, as expected from the predictions of GHD theory at the Euler scale.

The boundary profile, for clouds prepared with deep evaporative cooling, is in fair agreement with GHD predictions assuming the semi-infinite gas is in its ground state, although deviations are present. From the boundary profile, we show that it is in principle possible to reconstruct the rapidity distribution characterizing the initial gas. This protocol can thus be used as a generalized thermometry. However, the reconstruction method suffers from a high sensitivity to experimental noise in the tail of the boundary profile, which prevents us from re-

constructing faithfully the initial rapidity distribution. Instead, we use an Ansatz parametrized by a few parameters to extract the rapidity distributions of the initial gas from a fit to the boundary profile.

Finally, we use a newly developed technique [32] to probe the local rapidity distribution within the boundary. The latter is expected to be highly asymmetric for an initial state whose rapidity distribution is substantially broader and smoother than that of the ground state: while one of its borders reflects the broad character of the initial rapidity distribution, the other border presents the sharp feature expected for the ground state. Our experimental data show such an asymmetric behavior, although the sharp border presents an unelucidated tail.

2 Experimental setup

We produce an ultra-cold gas of ^{87}Rb bosonic atoms in the stretched state $|F = 2, m_F = 2\rangle$ using an atom chip. In addition to a homogeneous longitudinal magnetic field $B_0 = 3.36$G, transverse trapping is achieved with three parallel microwires deposited on the chip (shown in blue in Fig.1(a)) which carry AC currents modulated at 400MHz. This configuration eliminates wire roughness effects and allows independent control over both longitudinal and transverse confinement [33]. The atoms are trapped 7μm from the chip surface and 15μm from the wires, enabling strong transverse confinement. The transverse trapping potential is well approximated by a harmonic potential with a frequency of $\omega_\perp/2\pi = 2.56$kHz. Using radio-frequency evaporative cooling, we produce atomic clouds whose linear density n_0 is close to 50 at/μm. Further details on the setup can be found in [34]. The effective 1D coupling constant for atoms in the transverse ground state is given by $g = 2a_{3D}\hbar\omega_\perp$ [35], where $a_{3D} = 5.3$ nm is the 3D scattering length of ^{87}Rb [36]. The dimensionless Lieb parameter $\gamma = mg/(\hbar^2 n_0)$ lies in the range $[0.4, 0.7] \times 10^{-2}$ for the data presented in this paper, corresponding to an interaction energy gn_0 in $[0.4\hbar\omega_\perp, 0.6\hbar\omega_\perp]$. From our experience of radio-frequency cooling in our set-up [32,37], we expect the cloud to lie in the quasi-condensate regime [38], with a temperature ranging from about gn_0 to a few times gn_0.

The longitudinal magnetic trap is produced by DC currents running through four wires positioned on either side of the three microwires, as shown in the Fig.1(a). Since these wires are placed far from the atomic cloud, the longitudinal potential can be expanded as a Taylor series expansion $V(x) = \sum_i a_i x^i$. The four first coefficients a_i are tuned by adjusting the currents in the four wires that generate the longitudinal trapping potential. By carefully selecting these currents, it is possible to set a_1, a_2 and a_3 to zero such that the leading term is the quartic term $V(x) = a_4 x^4$. Such a potential permits to achieve a quasi-homogeneous atomic density over a relatively large region, an important feature to study the bipartite quench protocol which assumes a semi-infinite system. An example of linear density profile for an atomic cloud placed in such a potential is represented in gray in Fig.1(b). The linear density n_0 remains constant to within 10% around the peak density over a range of approximately 250μm.

To produce the initial bipartition, we use the selection method introduced in [32]. We illuminate the left border of the atomic cloud, initially in a global stationary state in a quartic trap, with a pushing beam that is nearly resonant with the $F = 2 \to F' = 3$ transition of the $D2$ line and which propagates perpendicularly to x. Atoms shined by this pushing beam are subjected to radiation pressure: after being illuminated for 30μs corresponding to ~ 15 absorption/reemission cycles, atoms have enough energy to leave the trap. To illuminate only a border of the gas, the beam is shaped using a digital micromirror device (DMD). Further details on this spatial selection method are available in [32]. This protocol produces a sharp boundary between a zero density system and a quasi-homogeneous gas due to the fact that the atoms are initially placed in a quartic trap. The sharpness of the boundary is mainly limited
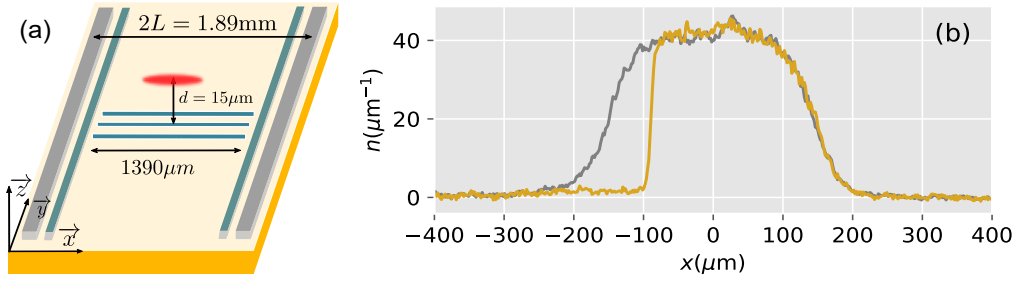
Figure 1: (a) Schematic drawing of the atom chip. The 3 blue wires produce the transverse trapping, the 4 other wires produce the longitudinal trapping. The red oval ball represents the atomic cloud, trapped 12 microns above the wires — (b) Linear density profiles extracted from absorption images. The gray curve is the linear density profile of gas confined within a quartic potential. The atomic cloud is then illuminated during $30\mu s$ by a near resonant light beam, shaped using a DMD. The resulting density profile after a time of flight of 1ms is depicted in yellow.

by the imaging resolution, which is in the micrometer range. The reabsorption of scattered photons by the atoms which are not shined could also limit the boundary sharpness. This effect is mitigated by detuning the pushing beam by 15MHz from the D2 transition. An example of the density profile of a gas initially in a global stationary state in a quartic trap, after applying this spatial selection tool, is shown in yellow in Fig.1(b).

The longitudinal confinement is then removed while maintaining the transverse confinement. The initial sharp boundary broadens in time and this dynamics is monitored by recording longitudinal density profiles $n(x,t)$ after different evolution time t.

3   GHD predictions

The above experimental setup is well described theoretically by the GHD approach [39, 40] which works as follows. Under time evolution, the initial sharp boundary of the cloud gets smoother, and the time derivatives of local quantities decrease. After some time, upon coarse-graining, one expects that the gas can locally be described by stationary states. Stationary states of the Lieb-Liniger model are entirely characterized by their rapidity distribution $\rho(\theta)$. Equivalently, they can be characterized by a function $\nu(\theta)$ dubbed 'occupation factor' which takes values between 0 and 1, and which is related to the rapidity distribution $\rho(\theta)$ by

$$\nu(\theta) = \frac{\rho(\theta)}{\rho_s(\theta)}, \qquad \text{where} \qquad \rho_s(\theta) = \frac{m}{2\pi\hbar} + \int \frac{d\theta'}{2\pi}\Delta(\theta - \theta')\rho(\theta'), \qquad (1)$$

and $\Delta(\Theta) = 2g/(g^2/\hbar + \hbar\Theta^2)$ is the 'scattering shift' in the Lieb-Liniger model. The functions ν and ρ are in one-to-one correspondence and in the following we use alternately ρ or ν. [For an introduction to this formalism, we refer to the lecture notes [41] or to Section 1 of the review article [30].]

Since we assume local stationarity, the system as a whole is described by a time- and position-dependent rapidity distribution $\rho(x,t,\theta)$, or equivalently by the time- and position-dependent occupation factor $\nu(x,t,\theta)$. The latter leads to simpler calculations, while the former is particularly useful to extract the linear density, which reads

$$n(x,t) = \int d\theta \, \rho(x,t,\theta). \qquad (2)$$
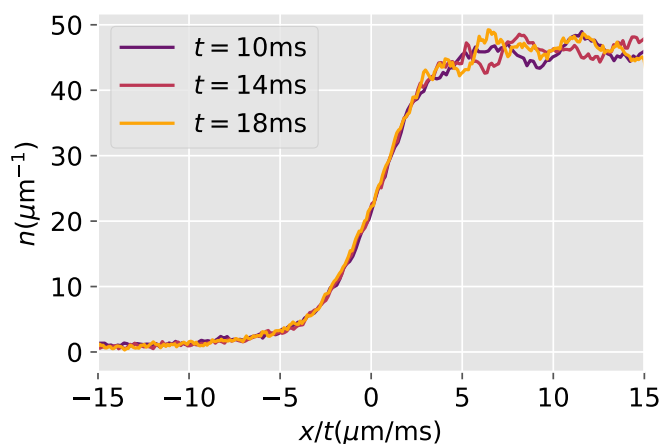
Figure 2: Test of the ballistic scaling. Boundary density profiles obtained for different evolution times t and plotted as a function of x/t. The profiles overlap remarkably well, showing that the Euler scale is reached within this time interval. The longitudinal dynamics after $t = 18$ms cannot be probed due to the fact that our initial semi-homogeneous gas has a finite size. For shorter deformation times, experimental boundary profiles are smoother than the Euler-scale GHD predictions, which might be due to the failure of Euler scale, and/or to the fact that the cut at $t = 0$ is not infinitely sharp.

The GHD equations [8, 9] predict the time evolution of $\rho(x, t, \theta)$, or equivalently of $\nu(x, t, \theta)$. When written in terms of the occupation factor $\nu(x, t, \theta)$, the GHD equations take the form of a convective equation

$$\frac{\partial \nu}{\partial t} + v^{\text{eff}}_{[\nu]} \frac{\partial \nu}{\partial x} = 0, \tag{3a}$$

and a second relation that fixes the effective velocity $v^{\text{eff}}_{[\nu]}$ as a functional of the local rapidity distribution,

$$v^{\text{eff}}_{[\nu]}(\theta) = \theta - \int \Delta(\theta - \theta') \left(v^{\text{eff}}_{[\nu]}(\theta) - v^{\text{eff}}_{[\nu]}(\theta') \right) \rho(\theta') d\theta'. \tag{3b}$$

More precisely, Eq. (3a) is the 'Euler-scale' form of GHD, a diffusionless equation that is valid at the large scales. Diffusive corrections that enter in the form of a Navier-Stokes-type term [28, 42–44], or even dispersive corrections [45], have also been studied theoretically. However, they are subleading and so far they have not been observed experimentally. We will see below that our experimental data obey the scaling collapse expected at the Euler scale (Fig. 2), so these effects seem to be negligible in our situation, at least for the analysis of the boundary profiles. This is also compatible with a recent theoretical study in the weakly interacting regime that has concluded that diffusive effects should be very small [46]. Therefore, in this paper we ignore the possibility of subleading diffusive effects (as well as all higher-order effects) in our modeling, and we stick to the Euler-scale GHD equation above.

For an initial bipartition whose discontinuity is located at $x = 0$, the solution of (3) depends on x and t only through the ratio $\zeta = x/t$ [8, 9]. Thus all local properties of the gas should depend only on the ratio ζ. In particular the density profile should be a function of ζ only. We have checked that our experimental data verify that ballistic scaling, see Fig. 2.

Let us now elaborate on the solution of Eq. (3). According to the above scaling, it is of the form

$$\nu(x, t, \theta) = \nu^*(x/t, \theta), \tag{4}$$
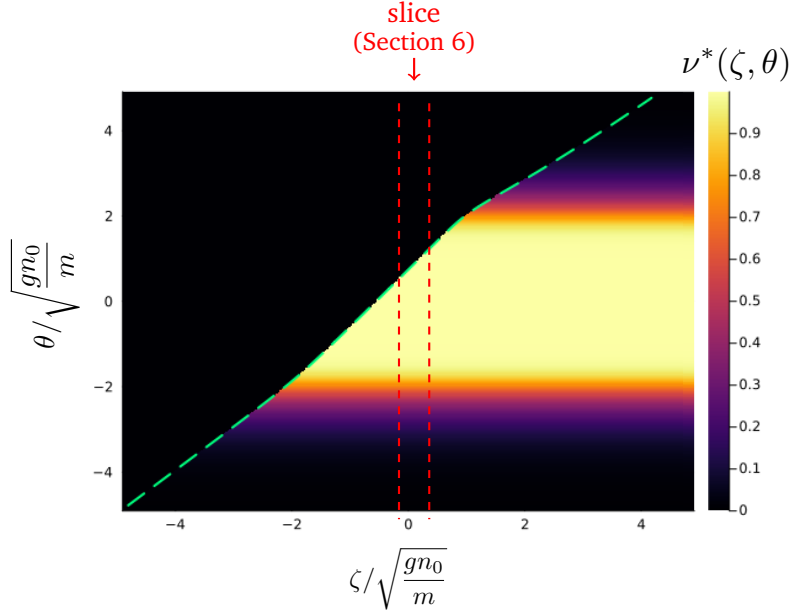
Figure 3: Occupation ratio $v^*(\zeta, \theta)$ solving the equation (5) for an initial occupation ratio $v_0(\theta)$ in the right half-system corresponding to thermal equilibrium at temperature T. The dashed green line is the curve $\theta^*(\zeta)$, *i.e.* it is the set of points (ζ, θ) such that $v^{\text{eff}}_{[v^*(\zeta,.)]}(\theta) = \zeta$. [Parameters: $\gamma_0 = mg/(n_0\hbar^2) = 0.005$, $k_B T\hbar^2/(mg^2) = 365$, close to the experimental parameters of the data set of Fig. 5.] The two vertical red dashed lines show a typical 'slice' of the boundary profile, which we study in detail in Section 6. In that slice, the occupation factor is highly asymmetric: it varies smoothly with θ for negative values of θ, while it behaves as a step function for θ close to θ^*.

for some function $v^*(x/t, \theta)$. For the situation considered in this paper with, initially, a vacuum state for $x < 0$ and a state of occupation factor $v_0(\theta)$ for $x > 0$, the solution $v^*(\zeta, \theta)$ is parameterized by an edge rapidity θ^* according to [8, 9]

$$v^*(\zeta, \theta) = \begin{cases} v_0(\theta), & \text{if} \quad \theta < \theta^*, \\ 0, & \text{if} \quad \theta > \theta^*, \end{cases} \quad \text{where} \quad v^{\text{eff}}_{[v^*(\zeta,.)]}(\theta^*) = \zeta. \tag{5}$$

This equation can be solved numerically for any given initial distribution $v_0(\theta)$, see Fig. 3 for an example. Together with Eq. (4), it entirely describes the system at the Euler scale. Note that, to compute the linear density $n(x, t)$ in order to compare with experimental density profiles, one uses Eq. (2).

4 Solution for a cloud initially in the ground state

To illustrate the above formalism, let us explore its implications for the special case where the right half-system is initially in the ground state. In that case the initial occupation factor $v_0(\theta)$ is a Fermi sea: $v_0(\theta) = 1$ for $|\theta| < \Delta\theta_0$, and $v_0(\theta) = 0$ otherwise. The Fermi radius $\Delta\theta_0$ depends on the initial linear density n_0 through Eq. (2) [29].

In that case the general features of the function $v^*(\zeta, \theta)$ that solves the GHD equation (3) are as follows (see Fig. 4). It comprises three regions: an 'empty region' far on the left with vanishing atom density, a 'filled region' far on the right where the density is equal to the initial density n_0, and a 'central region' where the atom density interpolates between 0 and n_0. It
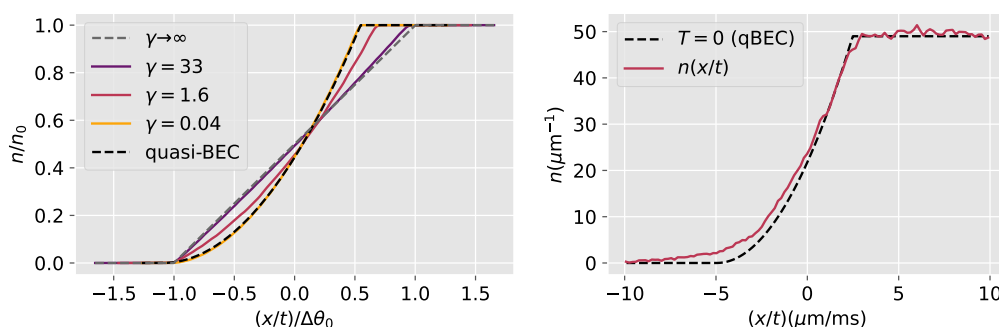
Figure 4: (a) Boundary profile predictions from GHD for system initially in the ground state as a function of γ. The velocity is normalized to the radius of the intial Fermi sea $\Delta\theta_0$. On the negative side the point where n reaches 0 is at $\Delta\theta_0$ whatever γ. On the positive side, the point where n reaches n_0 is at the speed of sound c. The black, resp. grey, dashed line corresponds to the hydrodynamic prediction in the quasi-BEC regime (Eq. (7)), resp. in the hard-core regime (Eq. (6)). (b) Comparison between experimental data and zero temperature prediction. The latter is given by eq. (7) with very good precision since the interaction parameter of the data is as low as $\gamma = 4.6 \times 10^{-3}$. [The experimental curve, recorded for an evolution time $t = 10$ ms, belongs to a different data-set than that used in Fig. 2.]

is easy to see that the left endpoint, where the atom density vanishes, is at $\zeta = -\Delta\theta_0$. The right endpoint velocity on the other hand is the sound velocity in the fluid of density n_0, given by $c = v_{[\nu_0]}^{\mathrm{eff}}(\Delta\theta_0)$. In the central region $-\Delta\theta_0 < x/t < c$, the gas is locally in a state that is a Fermi sea shifted by a Galilean boost of velocity $V(x/t)$ for some function V. For arbitrary interaction strengths g the density profile $n(x/t)$ cannot be computed in closed form, but it is easily computed numerically. Analytical expressions are available in the two asymptotic regimes of strong and weak interactions which correspond to $\gamma \gg 1$ and $\gamma \ll 1$ respectively.

In the strong repulsion regime, or hard-core regime, $v_{[\nu]}^{\mathrm{eff}}(\theta) = \theta$ regardless of the occupation factor $\nu(\theta)$. Then Eq.(5) is easily solved. We can use the fact that, in this regime, a Fermi sea of radius $\Delta\theta$ corresponds to a linear density $n = m\Delta\theta/(\pi\hbar)$ to derive

$$(\gamma \gg 1) \qquad n(x,t) = \frac{n_0}{2}\left(1 + \frac{xm}{t\pi\hbar n_0}\right), \qquad \text{if} \quad -\pi\hbar n_0/m < x/t < \pi\hbar n_0/m. \quad (6)$$

We can easily check that we recover the result expected for a gas of free fermions, as expected from the mapping of the hard-core bosons to fermions, which preserves the density [47].

In the weakly interacting regime, or quasi-BEC regime, the effective velocity at the edge of a Fermi sea of radius $\Delta\theta$ is $\Delta\theta/2$, in the frame where the Fermi sea is at rest. Then, using the fact that, in this regime, a Fermi sea of radius $\Delta\theta$ corresponds to a linear density $n = m\Delta\theta^2/(4g)$, we obtain

$$(\gamma \ll 1) \qquad n(x,t) = n_0\left(\frac{2}{3} + \frac{1}{3}\frac{x}{t}\sqrt{\frac{m}{gn_0}}\right)^2, \qquad \text{if} \quad -2\sqrt{gn_0/m} < x/t < \sqrt{gn_0/m}. \quad (7)$$

Here we recover the hydrodynamic predictions derived from the Gross-Pitaevskii equation [48, 49]. This is expected, since the Gross-Pitaevskii approach becomes exact in the limit of weak interactions, so it should agree with GHD, because GHD is the correct hydrodynamic equation for all repulsion strengths.

In Fig. 4(a), we compare the GDH solution for systems initially in the ground state with the two above asymptotic formulas. We find that the quasi-BEC regime is reached to an excellent approximation already for $\gamma = 0.04$.

Fig. 4(b) compares the measured boundary profile $n(\zeta)$ to the GHD prediction assuming that the initial state on the right is the ground state. Here the Lieb parameter is $\gamma = 4.6 \times 10^{-3}$, and for such small values the boundary profile is indistinguishable from the quasi-condensate prediction, see Fig. 4, so we actually compare the data to Eq. (7). The agreement between the ground state prediction and experimental data is rather good, especially in the high density part. The deviations from the parabola observed experimentally are due to non-zero entropy effects, which are investigated in the following section.

5 Retrieving the initial rapidity distribution from the boundary profile

In Section 3 we saw that, for a given initial occupation factor $v_0(\theta)$, we can compute the boundary profile $n(\zeta)$ with the Euler-scale GHD equations. Since, in the experiment, we measure the boundary profile, it is natural to ask whether the converse operation is possible: Can we retrieve the occupation factor $v_0(\theta)$ from the boundary profile, relying on the Euler-scale GHD equations?

Direct reconstruction. We assume that we have a boundary profile $n(v)$ which is monotonically increasing, with $n(\zeta) = 0$ when $\zeta \to -\infty$, and $n(\zeta) = n_0$ when $\zeta \to +\infty$. A first idea is to reconstruct the function $v_0(\theta)$ incrementally, from negative values of θ to positive ones, by 'reading' the boundary profile $n(\zeta)$ from left to right. We can start from some highly negative velocity ζ_0, such that $n(\zeta)$ is extremely small for all $\zeta \le \zeta_0$ so it can be assumed to (numerically) vanish: $n(\zeta) = 0$ for all $\zeta \le \zeta_0$. We work with discrete values of the rapidities, with a constant spacing $\delta\theta > 0$,

$$\theta_j = \zeta_0 + j\delta\theta, \qquad j \in \mathbb{N}, \tag{8}$$

and we reconstruct the corresponding values of the occupation factor v_j ($\simeq v_0(\theta_j)$) inductively. We initialize the sequence as

$$v_0 = 0. \tag{9}$$

At the jth step, all the occupation factors $v_0, v_1, \ldots, v_{j-1}$ are known, and we want to compute v_j. We fix v_j by requiring that

$$n(\zeta_j) = n_j, \tag{10}$$

where $n(\zeta)$ is the given boundary profile, and n_j and ζ_j are numerical estimates of the particle density and of the effective velocity respectively, obtained by discretizing the various integrals that enter the definitions of Section 3:

$$n_j = \sum_{a=0}^{j} \frac{\delta\theta}{2\pi} v_a 1_{j,a}^{\text{dr}} \quad \left(\simeq \int_{-\infty}^{\theta_j} \frac{d\theta}{2\pi} v(\theta) 1^{\text{dr}}(\theta) \right),$$

$$\zeta_j = \frac{\text{id}_{j,j}^{\text{dr}}}{1_{j,j}^{\text{dr}}} \quad \left(\simeq \frac{\text{id}^{\text{dr}}(\theta_j)}{1^{\text{dr}}(\theta_j)} \right).$$

Here $\text{id}(\theta) = \theta$ is the identity function, and the discretized dressed function f_j^{dr}, for a function f, is the solution of the linear system

$$f_{j,a}^{\text{dr}} = f(\theta_a) + \sum_{b=0}^{j} \frac{\delta\theta}{2\pi} \Delta(\theta_a - \theta_b) v_b f_{j,b}^{\text{dr}}.$$
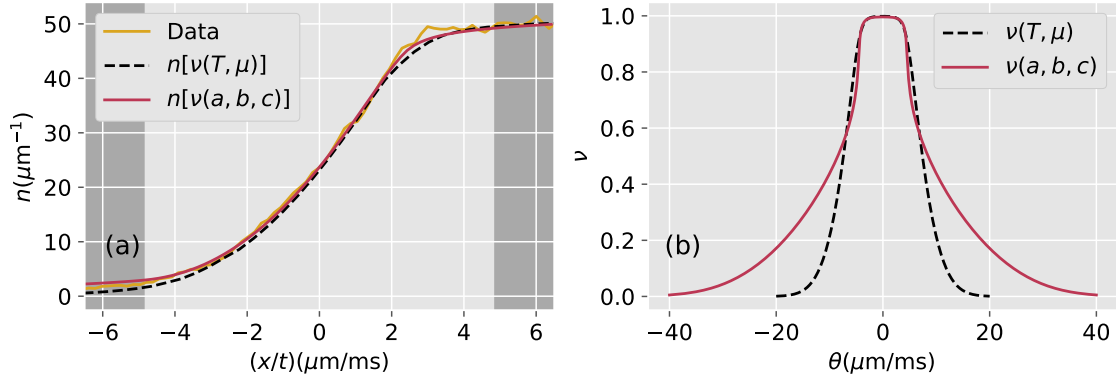
Figure 5: (a) The experimental boundary profile plotted in yellow is compared to fitted profiles using for $v_0(\theta)$ either a thermal Ansatz, *i.e.* the solution of Eqs. (11) and (12), (black dashed line) or the three-parameters Ansatz defined by Eqs.(11) and (13) (red line). The dark grey zones mark regions where the kinetic energy $m(x/t)^2/2$ is greater than the transverse energy gap $\hbar\omega_\perp$. Atoms with such kinetic energies might populate transversely excited states. Since almost all the boundary profile lies between these grey zones, one expects that the physics is well captured by the one-dimensional model. (b) Comparison of the occupation factors obtained for both fitted occupation factor distributions.

This is the discrete analog of the definition of the dressing, which is the solution of the integral equation $f^{dr}(\theta) = f(\theta) + \int_{-\infty}^{\theta_j} \frac{d\theta'}{2\pi}\Delta(\theta-\theta')v(\theta')f^{dr}(\theta')$ [see e.g. Refs. [30,41] for introductions to this formalism]. The value of v_j that fulfills Eq.(10) can be found numerically with a root-finding algorithm; we use the bisection method.

In the limit of small spacing $\delta\theta$, this procedure is expected to converge to a continuous occupation factor $v_0(\theta)$. Numerical tests presented in the appendix confirm that this method retrieves the correct $v_0(\theta)$.

However, when we try to apply this method to experimental boundary profiles, we face two difficulties. First, from spares and noisy experimental data points one needs to extract an increasing continuous function $n(\zeta)$. For this, we need to fit the data with some Ansatz for the boundary function. Second, we have observed that this method is highly sensitive to the details of the boundary profile $n(\zeta)$, especially to the left tail of $n(\zeta)$ at negative values of ζ. Since the signal-to-noise ratio in our experimental data is poor in this region, the results obtained with this technique are not trustworthy – see details in the appendix. Thus, we prefer to use an alternative method, which we present now.

Fitting the occupation factor $v_0(\theta)$. In order to extract the occupation factor distribution $v_0(\theta)$, we fit the experimental boundary profile with the GHD calculations based on Eqs. (4)-(5). Extracting $v_0(\theta)$ exactly would correspond to a fit with infinitely many fitting parameters, which we are not able to do. So we choose an Ansatz for $v_0(\theta)$, parameterized only by a few fitting parameters.

The first Ansatz that we try is the occupation factor of a Gibbs ensemble, where the fitting parameters are the temperature T and the chemical potential μ. This was calculated first by Yang and Yang [1], who showed that the occupation factor $v(\theta)$ is the solution of the integral equation

$$s'(v(\theta)) = \frac{a}{b} - \frac{m\theta^2}{2b} + \int d\theta' \Delta(\theta-\theta')[s(v(\theta')) - v(\theta')s'(v(\theta))], \qquad (11)$$

where $a = \mu$, $b = k_B T$, the function $s : [0 : 1] \to \mathbb{R}$ is

$$s(y) = -y \ln y + (1-y) \ln(1-y), \tag{12}$$

and s' is its derivative. The integral $\int s(\nu(\theta)) \rho_s(\theta) d\theta$ is the entropy per unit length of the occupation factor distribution $\nu(\theta)$ [1]. For a given T and μ, Eq. (11) can be solved numerically iteratively very efficiently using the fact that $s'^{-1}(\epsilon) = 1/(e^\epsilon + 1)$.

In Fig. 5 we compare the experimental boundary profile with the best fit obtained from this thermal equilibrium Ansatz. For the data set shown here, the fitted temperature and chemical potential are $T = 280 \pm 17 \text{nK}$ and $\mu/k_B = 71.5 \pm 0.7 \text{nK}$. The ratio $k_B T/\mu$ is noticeably larger than that usually found in our experiment when fitting the density profile of harmonically confined clouds since in the latter case $k_B T/\mu_0$, where μ_0 is the peak chemical potential takes values typically between 1 and 2 [32, 50]. We do not know where this discrepancy is coming from. It could originate from the fact that cooling in a quartic trap would be different from cooling in a harmonic trap.

The uncertainties in the fitting values of $T = 280 \pm 17 \text{nK}$ and $\mu/k_B = 71.5 \pm 0.7 \text{nK}$ are the standard deviation error obtained assuming that the discrepancy between the fit and the data is solely due to uncorrelated noise in the data points. However, discrepancy between the fit and the data shows some systematic effects, seen on all our datas, that indicate that the model does not faithfully describes the cloud: the left tail of the experimental data is wider than that of the fit while on the right side, the experimental date are more sharp. Interestingly, deviations from predictions for thermal states have already been observed for gases produced by evaporative cooling in an atom-chip setup [37, 50]: the phonons are found to have a lower temperature than the high-energy excitations, the latter coinciding with the presence of rapities of large absolute value, as shown in [51].

In order to obtain a better fit of the boundary profile, we relax the assumption that the initial could is at thermal equilibrium. Even if non-thermal, the cloud is however in a global stationarity stationary state, since the density profile of the trapped cloud is time-independent. General stationary states of the GHD equations in presence of a confining potential $V(x)$ have a local occupation factor distribution $\nu(x, \theta)$ which obeys Eq. (11) with a global 'temperature coefficient' b and a local 'chemical potential coefficient' $a(x) = a_0 - V(x)$, where a_0 is the central 'chemical potential'. However, general stationary states differ from thermal states by the choice of the 'entropy' function $s(y)$, which does not need to be given by Eq.(12), but can be an arbitrary function [52]. In the following, we generalize the thermal stationary state by modifying the function s as follows,

$$s(y) = -(1 + c y)(y \ln(y) + (1-y) \ln(1-y)), \tag{13}$$

where c, dimensionless, is a third fitting parameter (together with the coefficients a and b), which is vanishing for thermal states. The motivation for this Ansatz is the following. First, inspecting Eq.(11), one sees that modifying Eq. (12) using a global multiplicative factor α would keep a thermal state but with a temperature now equal to αb instead of b. Very naively the above Ansatz should tend to produce a "temperature" – in a loose sense– which depends on the occupation factor: the rapidities of large absolute value, whose occupation factor is small, would be at a different "temperature" as the bulk of the rapidity distribution whose occupation factor is close to one, a feature seen in [37].

We used the Ansatz Eq.(13) to fit our data. More precisely, we fit the experimental boundary profile with the prediction for an initial occupation factor ν_0 which is the one which obeys Eq. (11) with the function s defined in Eq.(13). The fit decreases the square distance to the data by 30 % compared to the thermal fit and it gives the optimal parameters $a/k_B = 74 \pm 0.2 \text{nK}$, $b/k_B = 480 \pm 20 \text{nK}$ and $c = 2.6 \pm 0.25$.

6 Local rapidity distribution within the boundary

For an initial state of the gas corresponding to a smooth occupation factor $\nu(\theta)$ —for instance a thermal state—, the occupation factor $\nu^*(x/t, \theta)$ at fixed ratio x/t is expected to be highly asymmetric as a function of θ, according to Eq.(5) and as illustrated in Fig 2. Indeed, on the right side – large θ – it has a jump discontinuity, similar to the one of the ground state occupation function, while on the left side – small θ – it is smooth. This feature of $\nu^*(x/t, \theta)$ induces a strong asymmetry of the expected rapidity distribution $\rho(x/t, \theta)$. To reveal such peculiar features of the local state of the gas within the boundary, we use the protocol introduced in Ref. [32] to probe the local rapidity distribution. This protocol uses a technique to select a small slice of the gas. The rapidity distribution of the selected slice is then measured performing a 1D expansion [40, 53–56]: after a sufficiently long 1D expansion one indeed expects that the density profile and the velocity distribution of the atoms become equal to the rapidity distribution [57]. To enhance the expected asymmetry of the local rapidity distribution, the data set used in this section corresponds to a cloud hotter than those used in the previous sections. The full experimental protocol is detailed below.

First, we let the gas expand for a time $t = 18$ ms, such that the boundary broadens and covers a large zone of $\sim 350 \mu m$, see Fig. 6(a). Then we select the slice of the gas that lies in an interval $[x_0 - \ell/2, x_0 + \ell/2]$, removing all atoms lying outside the slice with a pushing beam [32]. In Fig. 6(a) we show the density profile 1ms after the selection of the slice. The fit to a smoothened rectangular function gives $x_0 = 18 \mu m$. For calculations, the width ℓ will be determined using the number of selected atoms (see below). Finally, we let this slice expand in 1D for an expansion time τ, and then we measure the longitudinal density $\tilde{n}(x, \tau)$. The latter reflects the total rapidity distribution of the slice $\Pi(\theta) = \int_{x_0-\ell/2}^{x_0+\ell/2} \rho(x, \theta) dx$, because the asymptotic behavior as $\tau \to \infty$ is $\tau \tilde{n}(x, \tau) \simeq \Pi((x - x_0)/\tau)$. The expected asymmetry of Π is thus expected to induce an asymmetry of the density $\tilde{n}(x, \tau)$ as a function of the position x. We observe this asymmetry experimentally in our expansion profiles, as expected. This is shown in Fig. 6 (b) for an expansion time of $\tau = 30$ ms.

To go beyond this qualitative observation, we perform an Euler-scale GHD calculation of
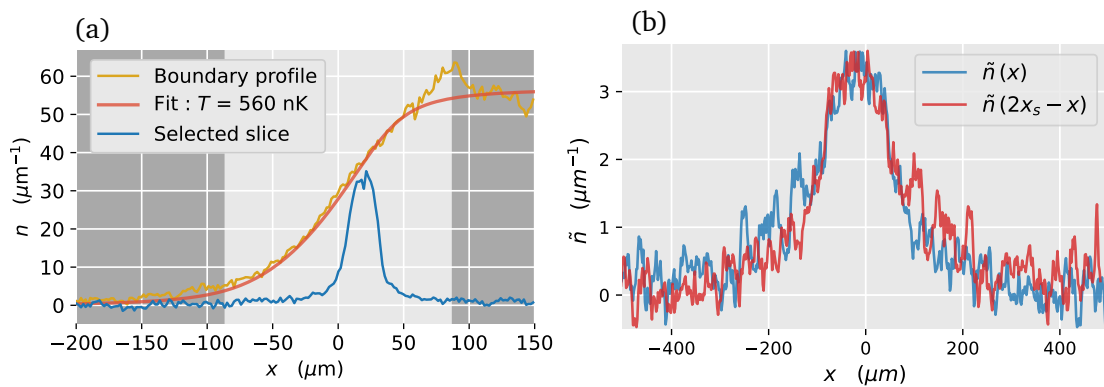
Figure 6: (a). *Boundary profile and selected slice.* The boundary profile after an evolution time $t = 18 \, ms$ is shown in solid yellow line. A thermal fit yielding $T = 560 \, nK$ is shown in orange. The density profile taken $1 \, ms$ after the slice selection is shown in blue. The dark grey area is the region where $m(x/t)^2/2 > \hbar\omega_\perp$. (b). *Asymmetry of the slice expansion profile.* The density profile after an expansion of the slice aver a time $\tau = 30$ ms is compared to its mirror image. The symmetry center $x_s = -17 \, \mu m$ is the point that minimises the curves square distance $\delta^2 = \int dx (\tilde{n}(x) - \tilde{n}(2x_s - x))^2$.

the expansion profile. Since here we are not interested in the exact shape of the smooth borders of the initial occupation factor $\nu_0(\theta)$, we simply model it by a thermal distribution. A fit of the boundary profile before the selection of the slice, shown in Fig. 6(a), yields $T = 560 \pm 22.5$ nK. Here we actually perform a one-parameter fit: the chemical potential is not a fit parameter, instead, for each temperature, the chemical potential is adjusted so that the linear density it corresponds to is the linear density in the region $x > 0$ measured before the boundary broadening. Starting from the initial sharp profile, we simulate both the boundary broadening and the slice expansion with GHD, assuming a perfect slicing, i.e. $\nu(x, \theta) = 0$ if $|x - x_0| > \ell/2$ and $\nu(x, \theta)$ is unchanged if $|x - x_0| < \ell/2$. The slice width ℓ is adjusted so that the calculated number of selected atoms equals the number of atoms in the experimental expansion profile, and we find $\ell = 24\,\mu$m.

The simulated expansion profile is shown in Fig. 7(a). It displays a strong asymmetry, as expected, with a sharp right edge and a vanishing density beyond a certain point on the right. The sharpness of this edge is, however, less pronounced than the one expected for the local rapidity distribution $\rho(x_0, \theta)$ at $x = x_0$, shown as dashed line in Fig. 7(a). Two effects contribute to the broadening of the edge. First the rapidity distribution is not homogeneous inside the slice and $\Pi(\theta)$ differs from $\ell\rho(x_0, \theta)$, as seen comparing the solid brown line and dashed line in Fig.7 (a). Second, the expansion time is finite and the expansion profile is not exactly $\Pi((x - x_0)/\tau)/\tau$, as seen comparing the red and brown solid lines in Fig.7 (a).

Next, we compare the expansion profile simulated with GHD to the experimental data. As shown in Fig 7(b), the predicted profile reproduces the main features of the experimental expansion profile. Discrepancy are however as large as 25% in the central part of the profile. The most striking difference between the measured profile and the expected one is the presence of tails in the right edge of the experimental profile – see the density profile in Fig.7(b). Such tails
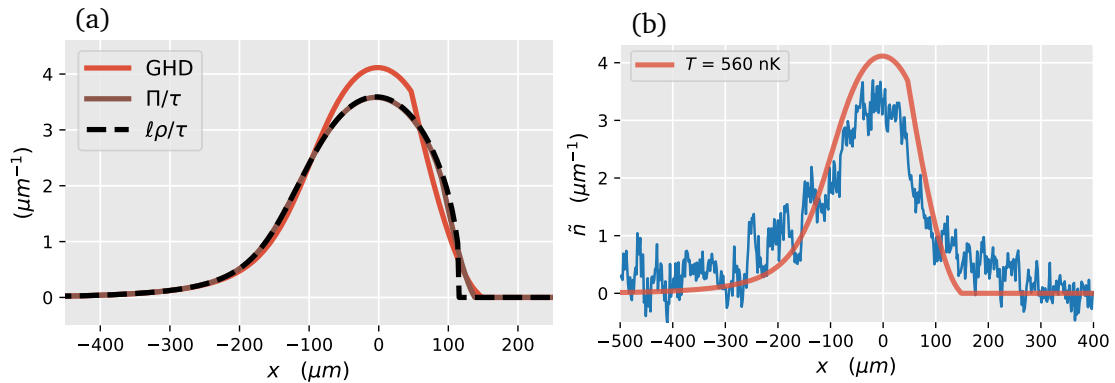
Figure 7: (a) *Density profile after slice expansion: effects of finite slice width and finite expansion time.* Orange line: GHD calculation of the density profile after an expansion of the slice for $\tau = 30$ ms, using as the initial temperature the value $T = 560$ nK obtained fitting the boundary profile. The brown line is the expected distribution if one assumes that the asymptotic large expansion time is reached, *i.e.* it shows $\Pi((x - x_0)/\tau)/\tau$, where $\Pi(\theta) = \int_{x_0-\ell/2}^{x_0+\ell/2} \rho(x, \theta)dx$ is the rapidity distribution of the selected slice. The black dashed line is $\ell\rho(x_0, (x - x_0)/\tau)/\tau$, which is the expected result in the limit of large τ and for a slice width ℓ negligible compared to the boundary extension. (b) *Comparison to experimental data.* Experimental data obtained after slice expansion during $\tau = 30$ ms (blue line) is compared to GHD calculations assuming an initial thermal state. The orange line, which is the same as in Fig.(a).

are absent from the Euler-Scale GHD calculations because the occupation factor distribution inside the slice strictly vanishes above a certain rapidity. The reason for the presence of such tails is unclear. It might be due to edge effects associated to the slicing procedure, atoms at the edges of the slice being heated by the pushing beam. There is also maybe an effect of diffusion that go beyond Euler-scale GHD: the diffusive term, neglected within Euler-scale GHD, could have an impact at the beginning of the edge deformation when gradients are large. Finally, we do not exclude that 3D effects are present since, for the data analysed in this section, a non vanishing fraction of the atoms do have a longitudinal energy larger than $\hbar\omega_\perp$. This is seen in Fig. 6 which shows that the boundary profile is non vanishing in the region $\zeta > \sqrt{2\hbar\omega_\perp/m}$. One possible way to investigate this would be to adapt the method of the collision integral developed in Ref. [58] to our setup (see also the discussion in Sec. 2.4.2 of the review [30]).

7 Conclusion

We have investigated experimentally the bipartite quench protocol for a gas of bosons strongly confined transversely. We have checked that the time evolution obeys the Euler hydrodynamic scaling since the density profile is found to be a function of x/t (Fig. 2). The density profile is close to the one predicted by the generalized hydrodynamic theory for the Lieb-Liniger gas at vanishing temperature, the latter coinciding with the Gross-Pitaevski prediction for the parameters of our data. The differences signal that the system is not in the ground state. We showed that the measurement of the boundary profile $n(v)$ could in principle permit the reconstruction of the occupation factor $\nu(\theta)$ of the initial gas, realizing a generalized thermometry method. However, in practice, we prefer to fit the observed boundary profile with the one obtained from generalized hydrodynamics using an Ansatz for the occupation factor. We have found that the measured boundary profiles are not very well accounted for by a thermal occupation factor, and we have considered more general occupation factors corresponding to stationary trapped clouds, which give a better fit with our data. Finally, we present measurement of the local rapidity distribution inside the boundary. The data show the expected asymmetry of the distribution. The distribution however shows noticeable differences compared to the GHD predictions, whose origin is not elucidated.

This work calls for further experimental investigations. In the near future we plan to compare the rapidity distributions obtained with the bipartite quench protocol by fitting the boundary profile to the rapidity distribution obtained using the slice expansion protocol [32]. Moreover, the temperatures obtained in this paper by the thermal fits are large so that the effects of populated transverse states might have an impact [58,59]. Thus it would be interesting to investigate clouds at smaller energies. The investigation of the local rapidity distribution within the boundary deserves further studies in order to elucidate the origin of the tails on the side that is expected to be effectively at vanishing entropy.

Acknowledgments

We thank V. Bulchandani for discussion about general stationary states of GHD in a confining potential and A. Urilyon and J. de Nardis for discussion about the possibility to observe diffusive effects. We also thank F. Nogrette, from LCF, for work on the installation of the DMD experiment and A.-L. Coutrot, from LCF, for reparation work on the chip.

Funding information We thank Sophie Bouchoule, Alan Durnez and Abdelmounaim Harouri of C2N laboratory for the chip fabrication. C2N is a member of RENATECH, the French national network of large facilities for micronanotechnology. This work was supported by ANR Project 'QUADY' ANR-20-CE30-0017-01 and by France 2030 in the framework of PEPR Quantique, Project 'DYN1D' ANR-23-PETQ-0001.

A   Appendix: Attempt at reconstructing the occupation factor from the boundary profile

In this appendix we elaborate on our attempt at reconstructing the occupation factor $\nu_0(\theta)$ from the boundary $n(\zeta)$, briefly reported in Section 5 in the main text.

First, we test the algorithm detailed in Section 5. For this we take a model occupation function of the form $1/(1 + e^{a\theta^2 - b})$, and compute the corresponding 'model boundary profile' $n(\zeta)$. Then we run our algorithm on this model boundary profile to reconstruct the occupation factor $\nu_0(\theta)$. We see in Fig. 8 that the reconstruction works as it should.

Next, we try to apply the algorithm to our experimental boundary profiles. We immediately face the following problem: The theoretical prediction for the boundary profile $n(\zeta)$ is necessarily monotonously increasing with ζ, while the experimental data are noisy so they can locally decrease. Therefore, in order to get a monotonously increasing function from our data, we start by fitting the data with a simple Ansatz of the form $a\,\mathrm{erfc}(-b*(\zeta-c))$, where erfc is the error function, see Fig. 9 (left panel). We have also tried to modify the Ansatz in order to
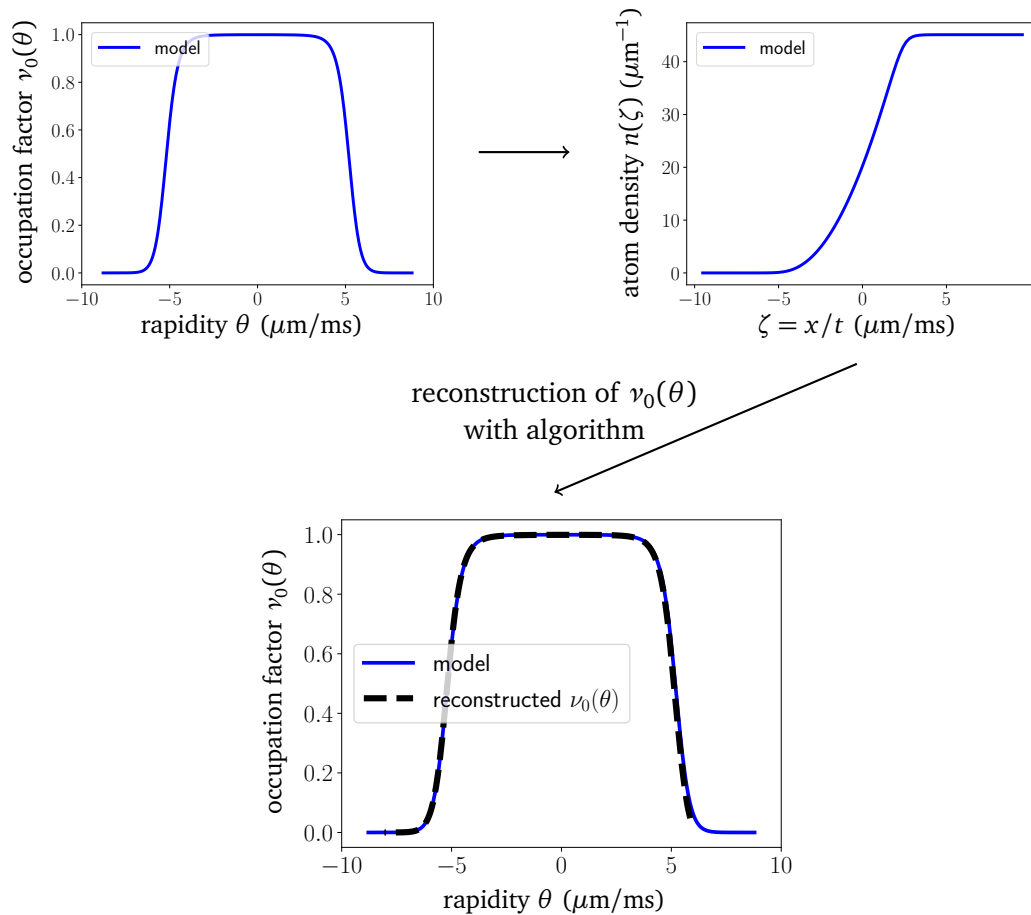
Figure 8: Test of the algorithm described in Section 5 on a model occupation ratio of the form $1/(1 + e^{a\theta^2 - b})$. Upper left: the model occupation ratio [Parameters: $a = 0.3\,\mathrm{ms}^2\,\mu\mathrm{m}^{-2}$ and $b = 8$.] Upper right: the corresponding boundary profile $n(\zeta)$. Bottom: the reconstructed occupation ratio obtained with the algorithm, compared with the model occupation factor. [The coupling constant g and atom mass m are the same as in the main text.]
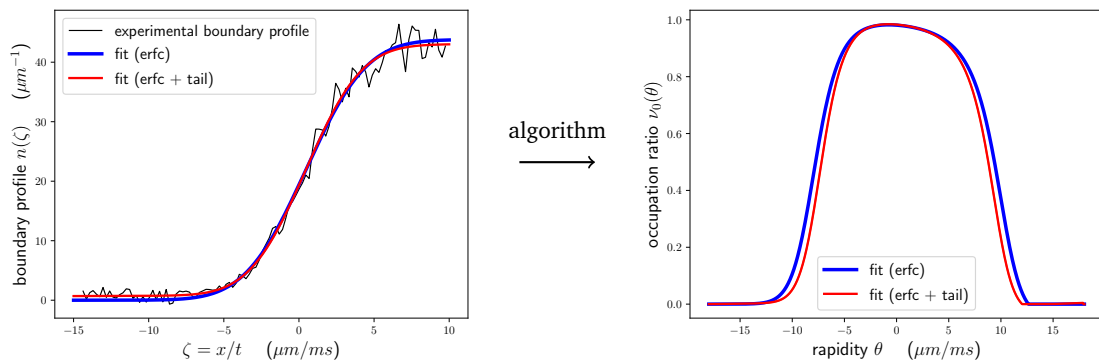
Figure 9: Left: fit of the experimental data for the density profile (noisy black line) with an error function $a\,\mathrm{erfc}(-b*(\zeta-c))$ (blue line) and with an error function plus a slowly decaying tail on the left, of the form $a\,\mathrm{erfc}(-b*(\zeta-c))-d/(\zeta-e)$. Right: the corresponding occupation factors reconstructed with the algorithm of Section 5. We conclude that the method is not satisfactory for our purposes: the reconstructed occupation ratio is in general not symmetric and is too sensitive to the details of the chosen Ansatz for the fit of the density profile.

allow for a slower decay of the tail for $\zeta < 0$, see Fig. 9. However the signal-to-noise ratio in our data does not allow us to discriminate between different choices of fit functions.

Once we have fitted the boundary profile $n(\zeta)$, we can run the algorithm on $n(\zeta)$ to find the corresponding occupation factor $\nu_0(\theta)$, see Fig. 9 (right). Unfortunately we find that this method is not satisfactory. The occupation ratio should be symmetric under $\theta \to -\theta$, but we can see in Fig. 9 (right) that it is not, with our choice of fit functions for $n(\zeta)$. Moreover we observe that the reconstructed occupation ratio is quite sensitive to the details of $n(\zeta)$. We have concluded that our data are too noisy to exploit this method, and this is the reason why we turn to the alternative method explained in the main text.

References

[1] C. N. Yang and C. P. Yang, *Thermodynamics of a one-dimensional system of bosons with repulsive delta-function interaction*, J. Math. Phys. **10**, 1115 (1969), doi:10.1063/1.1664947.

[2] A. B. Zamolodchikov, *Thermodynamic Bethe Ansatz in relativistic models: Scaling 3-state Potts and Lee-Yang models*, Nucl. Phys. B **342**, 695 (1990), doi:10.1016/0550-3213(90)90333-9.

[3] M. Rigol, V. Dunjko, V. Yurovsky and M. Olshanii, *Relaxation in a completely integrable many-body quantum System: An ab initio study of the dynamics of the highly excited states of 1D lattice hard-core bosons*, Phys. Rev. Lett. **98**, 050405 (2007), doi:10.1103/PhysRevLett.98.050405 [preprint doi:10.48550/arXiv.cond-mat/0604476].

[4] J. Mossel and J.-S. Caux, *Generalized TBA and generalized Gibbs*, J. Phys. A: Math. Theor. **45**, 255001 (2012), doi:10.1088/1751-8113/45/25/255001 [preprint doi:10.48550/arXiv.1203.1305].

[5] J.-S. Caux and R. M. Konik, *Constructing the generalized Gibbs ensemble after a quantum quench*, Phys. Rev. Lett. **109**, 175301 (2012), doi:10.1103/PhysRevLett.109.175301 [preprint doi:10.48550/arXiv.1203.0901].

[6] M. Fagotti and F. H. L. Essler, *Reduced density matrix after a quantum quench*, Phys. Rev. B **87**, 245107 (2013), doi:10.1103/PhysRevB.87.245107 [preprint doi:10.48550/arXiv.1302.6944].

[7] E. Ilievski, E. Quinn, J. De Nardis and M. Brockmann, *String-charge duality in integrable lattice models*, J. Stat. Mech.: Theory Exp. 063101 (2016), doi:10.1088/1742-5468/2016/06/063101 [preprint doi:10.48550/arXiv.1512.04454].

[8] B. Bertini, M. Collura, J. De Nardis and M. Fagotti, *Transport in out-of-equilibrium XXZ chains: Exact profiles of charges and currents*, Phys. Rev. Lett. **117**, 207201 (2016), doi:10.1103/PhysRevLett.117.207201 [preprint doi:10.48550/arXiv.1605.09790].

[9] O. A. Castro-Alvaredo, B. Doyon and T. Yoshimura, *Emergent hydrodynamics in integrable quantum systems out of equilibrium*, Phys. Rev. X **6**, 041065 (2016), doi:10.1103/PhysRevX.6.041065 [preprint doi:10.48550/arXiv.1605.07331].

[10] A. Bastianello, B. Bertini, B. Doyon and R. Vasseur, *Introduction to the special issue on emergent hydrodynamics in integrable many-body systems*, J. Stat. Mech.: Theory Exp. 014001 (2022), doi:10.1088/1742-5468/ac3e6a.

[11] B. Doyon, S. Gopalakrishnan, F. Møller, J. Schmiedmayer and R. Vasseur, *Generalized hydrodynamics: A perspective*, Phys. Rev. X **15**, 010501 (2025), doi:10.1103/PhysRevX.15.010501 [preprint doi:10.48550/arXiv.2311.03438].

[12] B. Riemann, *Ueber die Fortpflanzung ebener Luftwellen von endlicher Schwingungsweite*, in *Abhandlungen der Geselschaft der Wissenschaften zu Göttingen*, Göttingen, Germany (1860).

[13] J. De Nardis and M. Panfil, *Edge Singularities and quasilong-range order in nonequilibrium steady states*, Phys. Rev. Lett. **120**, 217206 (2018), doi:10.1103/PhysRevLett.120.217206 [preprint doi:10.48550/arXiv.1801.08079].

[14] D. X. Horváth, *Hydrodynamics of massless integrable RG flows and a non-equilibrium c-theorem*, J. High Energy Phys. **10**, 020 (2019), doi:10.1007/JHEP10(2019)020.

[15] V. Alba, B. Bertini and M. Fagotti, *Entanglement evolution and generalised hydrodynamics: Interacting integrable systems*, SciPost Phys. **7**, 005 (2019), doi:10.21468/SciPostPhys.7.1.005 [preprint doi:10.48550/arXiv.1903.00467].

[16] C. Rylands and P. Calabrese, *Transport and entanglement across integrable impurities from generalized hydrodynamics*, Phys. Rev. Lett. **131**, 156303 (2023), doi:10.1103/PhysRevLett.131.156303 [preprint doi:10.48550/arXiv.2303.01779].

[17] O. Gamayun, Y. Zhuravlev and N. Iorgov, *On Landauer-Büttiker formalism from a quantum quench*, J. Phys. A: Math. Theor. **56**, 205203 (2023), doi:10.1088/1751-8121/accabf [preprint doi:10.48550/arXiv.2211.08330].

[18] D. X. Horvath, B. Doyon and P. Ruggiero, *Full counting statistics after quantum quenches as hydrodynamic fluctuations*, (arXiv preprint) doi:10.48550/arXiv.2411.14406.

[19] S. Yuan, H. De Raedt and S. Miyashita, *Domain-wall dynamics near a quantum critical point*, Phys. Rev. B **75**, 184305 (2007), doi:10.1103/PhysRevB.75.184305 [preprint doi:10.48550/arXiv.0704.0193].

[20] T. Antal, Z. Rácz, A. Rákos and G. M. Schütz, *Transport in the XX chain at zero temperature: Emergence of flat magnetization profiles*, Phys. Rev. E **59**, 4912 (1999), doi:10.1103/PhysRevE.59.4912 [preprint doi:10.48550/arXiv.cond-mat/9812237].

[21] J. Hauschild, F. Heidrich-Meisner and F. Pollmann, *Domain-wall melting as a probe of many-body localization*, Phys. Rev. B **94**, 161109 (2016), doi:10.1103/PhysRevB.94.161109 [preprint doi:10.48550/arXiv.1605.05574].

[22] M. Collura, A. De Luca and J. Viti, *Analytic solution of the domain-wall nonequilibrium stationary state*, Phys. Rev. B **97**, 081111 (2018), doi:10.1103/PhysRevB.97.081111 [preprint doi:10.48550/arXiv.1707.06218].

[23] G. Misguich, N. Pavloff and V. Pasquier, *Domain wall problem in the quantum XXZ chain and semiclassical behavior close to the isotropic point*, SciPost Phys. **7**, 025 (2019), doi:10.21468/SciPostPhys.7.2.025 [preprint doi:10.48550/arXiv.1905.08756].

[24] S. Scopa, P. Calabrese and J. Dubail, *Exact hydrodynamic solution of a double domain wall melting in the spin-1/2 XXZ model*, SciPost Phys. **12**, 207 (2022), doi:10.21468/SciPostPhys.12.6.207 [preprint doi:10.48550/arXiv.2109.05249].

[25] M. Collura, A. De Luca, P. Calabrese and J. Dubail, *Domain-wall melting in the spin-1/2 XXZ spin chain: Emergent Luttinger liquid with fractal quasi-particle charge*, Phys. Rev. B **102**, 180409 (2020), doi:10.1103/PhysRevB.102.180409 [preprint doi:10.48550/arXiv.2001.04948].

[26] S. Scopa and D. Karevski, *Scaling of fronts and entanglement spreading during a domain wall melting*, Eur. Phys. J. Spec. Top. **232**, 1763 (2023), doi:10.1140/epjs/s11734-023-00845-1 [preprint doi:10.48550/arXiv.2303.10054].

[27] A. J. McRoberts, T. Bilitewski, M. Haque and R. Moessner, *Domain wall dynamics in classical spin chains: Free propagation, subdiffusive spreading, and soliton emission*, Phys. Rev. Lett. **132**, 057202 (2024), doi:10.1103/PhysRevLett.132.057202 [preprint doi:10.48550/arXiv.2306.15351].

[28] J. De Nardis, D. Bernard and B. Doyon, *Diffusion in generalized hydrodynamics and quasiparticle scattering*, SciPost Phys. **6**, 049 (2019), doi:10.21468/SciPostPhys.6.4.049 [preprint doi:10.48550/arXiv.1812.00767].

[29] E. H. Lieb and W. Liniger, *Exact analysis of an interacting Bose gas. I. The general solution and the ground state*, Phys. Rev. **130**, 1605 (1963), doi:10.1103/PhysRev.130.1605.

[30] I. Bouchoule and J. Dubail, *Generalized hydrodynamics in the one-dimensional Bose gas: Theory and experiments*, J. Stat. Mech.: Theory Exp. 014003 (2022), doi:10.1088/1742-5468/ac3659 [preprint doi:10.48550/arXiv.2108.02509].

[31] P. Schüttelkopf, M. Tajik, N. Bazhan, F. Cataldini, S.-C. Ji, J. Schmiedmayer and F. Møller, *Characterizing transport in a quantum gas by measuring Drude weights*, Science eads8327 (2025), doi:10.1126/science.ads8327.

[32] L. Dubois, G. Thémèze, F. Nogrette, J. Dubail and I. Bouchoule, *Probing the local rapidity distribution of a one-dimensional Bose gas*, Phys. Rev. Lett. **133**, 113402 (2024), doi:10.1103/PhysRevLett.133.113402 [preprint doi:10.48550/arXiv.2312.15344].

[33] J.-B. Trebbia, C. L. Garrido Alzar, R. Cornelussen, C. I. Westbrook and I. Bouchoule, *Roughness suppression via rapid current modulation on an atom chip*, Phys. Rev. Lett. **98**, 263201 (2007), doi:10.1103/PhysRevLett.98.263201.

[34] L. Dubois, *Dynamique hors d'équilibre d'un gaz de Bosons unidimensionnel étudiée via la mesure spatialement résolue de la distribution des quasiparticules*, PhD thesis, Université Paris-Saclay, Paris, France (2024).

[35] M. Olshanii, *Atomic scattering in the presence of an external confinement and a gas of impenetrable bosons*, Phys. Rev. Lett. **81**, 938 (1998), doi:10.1103/PhysRevLett.81.938 [preprint doi:10.48550/arXiv.cond-mat/9804130].

[36] A. Marte, T. Volz, J. Schuster, S. Dürr, G. Rempe, E. G. M. van Kempen and B. J. Verhaar, *Feshbach resonances in rubidium 87: Precision measurement and analysis*, Phys. Rev. Lett. **89**, 283202 (2002), doi:10.1103/PhysRevLett.89.283202 [preprint doi:10.48550/arXiv.cond-mat/0210651].

[37] A. Johnson, S. S. Szigeti, M. Schemmer and I. Bouchoule, *Long-lived nonthermal states realized by atom losses in one-dimensional quasicondensates*, Phys. Rev. A **96**, 013623 (2017), doi:10.1103/PhysRevA.96.013623 [preprint doi:10.48550/arXiv.1703.00322].

[38] K. V. Kheruntsyan, D. M. Gangardt, P. D. Drummond and G. V. Shlyapnikov, *Pair correlations in a finite-temperature 1D Bose gas*, Phys. Rev. Lett. **91**, 040403 (2003), doi:10.1103/PhysRevLett.91.040403 [preprint doi:10.48550/arXiv.cond-mat/0212153].

[39] M. Schemmer, I. Bouchoule, B. Doyon and J. Dubail, *Generalized hydrodynamics on an atom chip*, Phys. Rev. Lett. **122**, 090601 (2019), doi:10.1103/PhysRevLett.122.090601 [preprint doi:10.48550/arXiv.1810.07170].

[40] N. Malvania, Y. Zhang, Y. Le, J. Dubail, M. Rigol and D. S. Weiss, *Generalized hydrodynamics in strongly interacting 1D Bose gases*, Science **373**, 1129 (2021), doi:10.1126/science.abf0147 [preprint doi:10.48550/arXiv.2009.06651].

[41] B. Doyon, *Lecture notes on generalised hydrodynamics*, SciPost Phys. Lect. Notes 18 (2020), doi:10.21468/SciPostPhysLectNotes.18 [preprint doi:10.48550/arXiv.1912.08496].

[42] J. De Nardis, D. Bernard and B. Doyon, *Hydrodynamic diffusion in integrable systems*, Phys. Rev. Lett. **121**, 160603 (2018), doi:10.1103/PhysRevLett.121.160603 [preprint doi:10.48550/arXiv.1807.02414].

[43] A. Bastianello, A. De Luca, B. Doyon and J. De Nardis, *Thermalization of a trapped one-dimensional Bose gas via diffusion*, Phys. Rev. Lett. **125**, 240604 (2020), doi:10.1103/PhysRevLett.125.240604 [preprint doi:10.48550/arXiv.2007.04861].

[44] J. De Nardis, B. Doyon, M. Medenjak and M. Panfil, *Correlation functions and transport coefficients in generalised hydrodynamics*, J. Stat. Mech.: Theory Exp. 014002 (2022), doi:10.1088/1742-5468/ac3658 [preprint doi:10.48550/arXiv.2104.04462].

[45] J. De Nardis and B. Doyon, *Hydrodynamic gauge fixing and higher order hydrodynamic expansion*, J. Phys. A: Math. Theor. **56**, 245001 (2023), doi:10.1088/1751-8121/acd153 [preprint doi:10.48550/arXiv.2211.16555].

[46] F. Møller, F. Cataldini and J. Schmiedmayer, *Identifying diffusive length scales in one-dimensional Bose gases*, SciPost Phys. Core **7**, 025 (2024), doi:10.21468/SciPostPhysCore.7.2.025 [preprint doi:10.48550/arXiv.2312.14007].

[47] M. Girardeau, *Relationship between systems of impenetrable bosons and fermions in one dimension*, J. Math. Phys. **1**, 516 (1960), doi:10.1063/1.1703687.

[48] G. A. El, V. V. Geogjaev, A. V. Gurevich and A. L. Krylov, *Decay of an initial discontinuity in the defocusing NLS hydrodynamics*, Phys. D: Nonlinear Phenom. **87**, 186 (1995), doi:10.1016/0167-2789(95)00147-V.

[49] G. Xu, M. Conforti, A. Kudlinski, A. Mussot and S. Trillo, *Dispersive dam-break flow of a photon fluid*, Phys. Rev. Lett. **118**, 254101 (2017), doi:10.1103/PhysRevLett.118.254101 [preprint doi:10.48550/arXiv.1703.09019].

[50] B. Fang, *Equilibrium and nonequilibrium behaviours of 1D Bose gases*, PhD thesis, Institut d'Optique Graduate School, Palaiseau, France (2014).

[51] I. Bouchoule and J. Dubail, *Breakdown of Tan's relation in lossy one-dimensional Bose gases*, Phys. Rev. Lett. **126**, 160603 (2021), doi:10.1103/PhysRevLett.126.160603 [preprint doi:10.48550/arXiv.2011.13250].

[52] V. B. Bulchandani, *Revised Enskog equation for hard rods*, J. Stat. Mech.: Theory Exp. 043205 (2024), doi:10.1088/1742-5468/ad3ccd [preprint doi:10.48550/arXiv.2309.15846].

[53] J. M. Wilson, N. Malvania, Y. Le, Y. Zhang, M. Rigol and D. S. Weiss, *Observation of dynamical fermionization*, Science **367**, 1461 (2020), doi:10.1126/science.aaz0242 [preprint doi:10.48550/arXiv.1908.05364].

[54] K. Yang, Y. Zhang, K.-Y. Li, K.-Y. Lin, S. Gopalakrishnan, M. Rigol and B. L. Lev, *Phantom energy in the nonlinear response of a quantum many-body scar state*, Science **385**, 1063 (2024), doi:10.1126/science.adk8978.

[55] K.-Y. Li, Y. Zhang, K. Yang, K.-Y. Lin, S. Gopalakrishnan, M. Rigol and B. L. Lev, *Rapidity and momentum distributions of one-dimensional dipolar quantum gases*, Phys. Rev. A **107**, L061302 (2023), doi:10.1103/PhysRevA.107.L061302 [preprint doi:10.48550/arXiv.2211.09118].

[56] M. Horvath, A. Bastianello, S. Dhar, R. Koch, Y. Guo, J.-S. Caux, M. Landini and H.-C. Nägerl, *Observing Bethe strings in an attractive Bose gas far from equilibrium*, (arXiv preprint) doi:10.48550/arXiv.2505.10550.

[57] A. S. Campbell, D. M. Gangardt and K. V. Kheruntsyan, *Sudden expansion of a one-dimensional Bose gas from power-law traps*, Phys. Rev. Lett. **114**, 125302 (2015), doi:10.1103/PhysRevLett.114.125302 [preprint doi:10.48550/arXiv.1501.01896].

[58] F. Møller, C. Li, I. Mazets, H.-P. Stimming, T. Zhou, Z. Zhu, X. Chen and J. Schmiedmayer, *Extension of the generalized hydrodynamics to the dimensional crossover regime*, Phys. Rev. Lett. **126**, 090602 (2021), doi:10.1103/PhysRevLett.126.090602 [preprint doi:10.48550/arXiv.2006.08577].

[59] F. Cataldini, F. Møller, M. Tajik, J. Sabino, S.-C. Ji, I. Mazets, T. Schweigler, B. Rauer and J. Schmiedmayer, *Emergent Pauli blocking in a weakly interacting Bose gas*, Phys. Rev. X **12**, 041032 (2022), doi:10.1103/PhysRevX.12.041032 [preprint doi:10.48550/arXiv.2111.13647].